DELFT UNIVERSITY OF TECHNOLOGY

MASTER THESIS

The Development of a Micromodel Protocol followed by a Study of Oil Mobilization in the Micromodel

M.J.E.J. Hurkmans

supervised by:
C.P.J.W. van Kruijsdijk, TU Delft
F.S.H. Al Saadi, TU Delft
K.H.A.A. Wolf, TU Delft

May 12, 2017

Title	:	The Development of a Micromodel Protocol followed by a Study of Oil Mobilization in the Micromodel
Author(s)	:	M.J.E.J. Hurkmans
Date	:	May 12, 2017
Professor(s)	:	Prof. Ir. C.P.J.W. van Kruijsdijk.
Supervisor(s)	:	Msc. F.S.H. Al Saadi
	:	Dr. K.H.A.A. Wolf
Committee member	:	Prof. Dr. J. Bruining

Postal Address	:	Section for Petroleum Engineering Department of Geoscience & Engineering Delft University of Technology P.O. Box 5048 The Netherlands
Telephone	:	(31) 15 2781328 (secretary)
Telefax	:	(31) 15 2781189

The Development of a Micromodel Protocol followed by a Study of Oil Mobilization in the Micromodel

Martijn Hurkmans

ABSTRACT – In the development of EOR techniques in the field, the visualization and characterization on the different flow regimes within the system continues to be investigated. In this study an attempt was made to visualize the creation of an oilbank with the help of micromodels. Micromodels have been used in the past, but there were some limits to it. Their structures can be complex and heterogeneous as in the field, yet the limit is the short pathways.
The micromodel that was used for this study had the properties of the Fountainbleau rock with a total pathway of 79 cm. A custom made setup was developed to ensure that a desired dynamic fluid flow process was achieved. A protocol for executing the experiments was made in order to achieve the optimal conditions and reproduce the experiments over time. The experiments were conducted in UV-light. As the oil was dyed with Nile-Red the UV-light allowed to distinguish the oil phase from the other phases during the experiments. A mimic of reservoir saturation was realized within the micromodel and an average initial oil saturation of 61 % was determined. Subsequently, the micromodel was waterflooded and the oil recovery factor, oil ganglia size distribution and entrapment mechanism of the residual oil were determined. Over the different channels of the micromodel an average recovery factor of 21 % and a residual oil saturation of 40 % were realized. Furthermore the frequency of smaller oil ganglia increases after waterflooding, mostly caused by the by-passing entrapment mechanism.
A phase behaviour study of the surfactant-polymer (SP) solution and the oil was carried out. The SP solution was made from Endoret-O242 surfactant and polymer HPAAM-3630. The surfactant and the oil form a fluid microemulsion and eventually leading to a change in interfacial tension properties. The study was carries out with different SP-compositions by changing the concentrations of salt, surfactant and SBA (2-butanol). The optimum was achieved with a salinity of 4 %, a surfactant concentration of 0.5 % w/w and a SBA concentration of 4 %.
The visualization of the oilbank was not successful. The microemulsion and SP-solution had a white appearance causing the UV-light to be reflected. Due to this reflection it was not possible to distinguish between the Nil-Red dyed oil and the SP-solution, and thus not possible to visualize the oilbank.

1. INTRODUCTION

Over the years oil is produced in multiple ways. First there was primary production, which uses the reservoir natural energy, fluid and rock expansion, solution-gas drive, gravity drainage, and aquifer influx for oil production. Later on waterflooding, a secondary production method, was introduced, whereby the driving force is the injection of water in the reservoir. When the oilfield reaches the end of its normal life after conventional recovery (primary and secondary), there is on average still $60 - 70\%$ of the initial oil in-place, which is known as remaining (combination of residual and by-passed) oil. Estimates (made in the late 1970s) of worldwide oil in-place range up to 1.5 trillion barrels; hence it is estimated that the oil remaining after conventional recovery would be approximately 1.0 trillion barrels. [Council and on Enhanced Recovery Techniques 1976] The recovery of this remaining oil is of great interest to the oil companies. Thus the past few decades the oil industry evolved to tertiary recovery, enhanced oil recovery (EOR), in order to recover the remaining oil. It has the benefit of continuous use of the existing installation of the primary and secondary techniques. EOR encompasses a range of different techniques, such as chemical, thermal and gas injection. [Stosur et al. 2003].
In this paper the chemical flooding is studied, more specific the surfactant-polymer (SP) flooding. This chemical EOR technique involves the injection of surfactants into the reservoir to reduce interfacial tension between oil and water and thus reduce capillary pressure for easier and better mobilization of oil. Polymers are also injected alongside to reduce the mobility ratio and gather the oil droplet within the reservoir to create an oil bank and mobilize the oil within the reservoir.
Normally, research on different EOR techniques is done in a specific order as can be seen in figure 1; this protocol is developed by Shell, and goes from lab via core flows to full field application.

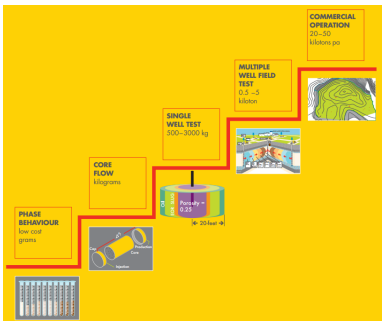

Fig. 1. Visualization of Shells policy on applying EOR to an oilfield. [Shell-Chemicals 2015]

The procedure Shell and other oil companies are applying does not allow to see what happens at microscopic level. In order to see the phase behavior on microscopic level with the surfactant-polymer flooding, the experiments in this paper are done with the use of a micromodel. Applying this method, gives the possibility to visualize the formation of the residual oil, as well the creation of a new oil bank by the use of SP-flooding.

This section gives an introduction to the entrapment of oil, SP flooding with respect to surfactants and polymers, and the use of micromodels. The remainder of this paper is organized as follows: Section 2, Research Objectives; Section 3, Micromodel Experiments; Section 4, Formation of Residual Oil ; Section 5, Analysis of Residual Oil; Section 6, Surfactant Behaviour; Section 7, Creation of Oilbank; Section 8, Recommendations & Discussion; Section 9, Conclusion.

1.1 Introduction to Entrapment

Secondary recovery by waterflooding leads to entrapment of oil as a result of capillary action in strongly wetting conditions, which are assumed throughout the rest of the work. The entrapment is associated with the ratio of viscous to capillary forces. This ratio is expressed as a dimensionless number called the Capillary number $[N_c]$

$$N_c = \frac{\mu v}{\sigma} \tag{1}$$

Where μ is the viscosity of the displacing fluid, σ is the interfacial tension (IFT) between the two fluid phases and v is the superficial velocity. The Capillary number represents the viscous forces versus the surface tension acting across an interface between two immiscible liquids. [Moore and Slobod 1956], [Taber et al. 1969], [Abrams et al. 1975], [Morrow et al. 1988]. Up to this point, the forces that have influence on two fluids are discussed. Now let us ask how the mechanism works by entrapping residual oil through waterflooding, where the fluid properties play a role, the structure of the pore, the pore geometry and the pore topology.

At first there is the snap-off mechanism, which has been modelled and described as Choke-off by Roof [Roof et al. 1970]. During snap-off, wetting fluid starts swelling until the non-wetting fluid interface becomes unstable, at which point the node or bond becomes entirely filled with wetting fluid, see figure 2

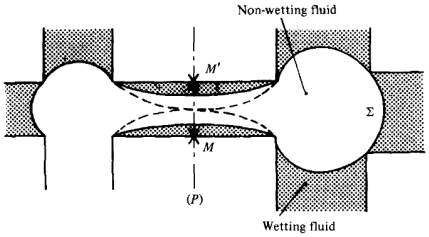

Fig. 2. Snap-off (choke-off) displacement mechanism. The wetting fluid is swelling to form a collar and then cause the non-wetting fluid to snap-off [Lenormand et al. 1984]

The snap-off is the result of capillary instability; if capillary pressure declines in throat, liquid accumulates and snap-off may occur. [Lenormand et al. 1983] [Stegemeier 1977] [Roof et al. 1970] Also the amount of snap-off increases with increasing Capillary number and decreasing wetting phase viscosity.[Al-Gharbi and Blunt 2005]

A second entrapment mechanism is bypassing. This phenomena is based on the Capillary pressure equation 2

$$\mathbf{P_C} = \frac{\mathbf{2}\sigma}{\mathbf{w/2}} = \frac{\mathbf{4}\sigma}{\mathbf{w}} \tag{2}$$

When the non-wetting displacement has the choice of two pathways, it tends to invade the larger pores because of the lower capillary pressure. [Chatzis and Dullien 1983] [Laidlaw and Wardlaw 1983] This tendency has been proven by the use of a pore doublet with a wide and narrow branch. See figure 3

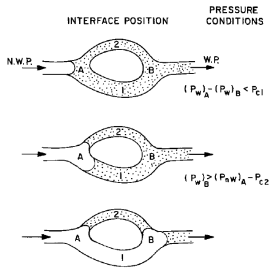

Fig. 3. Conventional pore doublet model representation of drainage-type of displacement [Chatzis and Dullien 1983]

Figure 3 displays drainage displacement, where the non-wetting phase displaces the wetting phase. With imbibition, the wetting phase displaces the non-wetting phase out of the reservoir, which can be observed in the pore doublet of figure 4

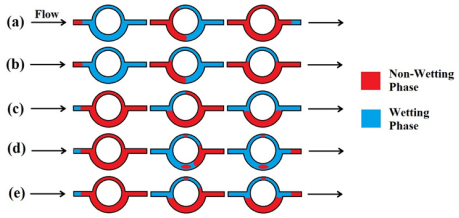

Fig. 4. illustrates the drainage and imbibition mechanisms for the pore doublet model. (a) Drainage Process, No Trapping ;(b) Drainage Process, Bypassing in Smaller Throat ;(c) Imbibition Process, Bypassing in Larger Throat ;(d) Imbibition Process, Snap-Off ;(e) Process, Snap-Off in Smaller Throat and Bypassing in Larger Throat [PERM-Inc 2013]

That bypassing happens in the larger pore during the imbibition can be found by using the capillary and viscous forces formula. These governing equations are based on the pore doublet model from Chatzis et al. See Appendix A.

The third entrapment mechanism is called the Jamin effect [Jamin 1860]. The Jamin effect may be defined as the resistance to flow under pressure through a capillary tube, which is encountered by liquid droplets that form a blockage [Smith and Crane 1930], as shown in Figure 5

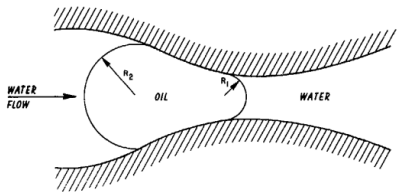

Fig. 5. Oil droplet that entering a pore constriction [McAuliffe et al. 1973]

Thus the Jamin effect is caused by the fact that the radius of curvature of a droplet entering a pore throat is smaller than that of the droplet in a pore body [McAuliffe et al. 1973]. It can cause the complete blockage of a pore throat, causing the flow to follow new paths. In order to overcome this blockage a pressure is required

to force the droplet through the pore throat and exits the capillary pressure difference. The governing equation can be found in Appendix A.

1.2 Introduction to Surfactant

Surfactant is an general word for surface active agents. The surfactant molecule is made out of polar water-soluble group and a non-polar water-insoluble hydrocarbon group, which makes it amphiphilic. Due to the its amphiphilic behaviour, a surfactant can lower the surface tension of a liquid, allowing easier spreading of the liquid. Also the interfacial tension between two liquids is reduced. [Thomas et al. 1999]
Surfactants allow the residual oil to move again, as they reduce the oil-water IFT and therefore influence the capillary number, making it large enough to overcome the capillary forces [Chatzis et al. 1984]. It is not a new idea and has already been applied in 1927 [Uren et al. 1927]. In order to have a successful displacement process, it firstly has to have a high enough reduction in the IFT between the water and oil in order to mobilize the residual oil. Secondly it has to maintain that reduction in the IFT throughout the reservoir in order to prevent the mobilized residual oil from being retrapped by capillary forces. [Shah 2012] The surfactant forms a microemulsion between the oil and water phase. These microemulsions are thermodynamically stable, which makes them suitable for pushing oil through porous media as it forms an in-situ situation. This technique was popular in the 1970s and 80s, yet it was not very economically beneficial due to the high concentration of surfactant that was needed. Nowadays better surfactant solutions can be made and therefore a lower concentration is needed.
Because of the well-established relationship between microemulsions, phase behaviour and IFT, the industry has developed new surfactant formulations [Levitt et al. 2006] [Shah 1981].

1.3 Introduction to Polymer

Polymer flooding has been applied for over 40 years. This method evolves in chemical EOR and has 3 major subjects: Polymer flooding, Surfactant Polymer flooding (SP) and Alkaline Surfactant Polymer flooding. They have been shown to be effective in recovering unswept oil by improving the mobility ratio. [Abidin et al. 2012] Over the past decades different polymers were established. At first there where water soluble polymers to increase the viscosity of the injected water. A lot of research was done to improve these polymers. After 1964, field test results and other significant laboratory studies made it possible to develop polymer flooding as a method to enhance oil recovery. [Mungan et al. 1966] [Shah 2012] In this research project the focus is on SP flooding. As described above the surfactant makes the residual oil more mobile due to its capability of lowering the IFT between the fluids. Still the surfactant follows the waterflooding path as it seeks the path of least resistance to the lower pressure region. This means that sequentially surfactant is injected, polymer slug is injected and water is injected. A characteristic of the polymer is that it is a very viscous fluid, which changes the mobility ratio. It is desired that the mobility ratio has a value of one or slightly less, as the efficiency of the displacement of the movable residual oil due to the surfactant is then the highest. Even a piston-like displacement can then be achieved. [Gogarty et al. 1967]

1.4 Introduction to micromodels

Micromodel is a porescale model that can accurately capture the physical and chemical processes that control transverse mixing and reaction in microfluidic pore structures. It is a device used for scientific purposes and has an interest to fields like biology, chemistry, physics, medicine and biomedical sciences. It consists of channels, pores and pore throats with a dimension of one micrometer to several hundred micrometers. It is a microfluidic system that has a volume of one nanoliter to several microliters. The advantage is that it enables you to directly evaluate the effects of porous media geometry on a transverse mixing-limited chemical reaction. With the micromodel it is possible to mimic what is happening within a coreflow experiment and it can be used several times. Also a more detailed study can be made for EOR, thus understanding the fluid behaviour with the use of the EOR technique on pore scale level. Most micromodels are built homogenous or with a repeating pattern. In order to mimic reservoir condition a micromodel has been developed with the properties of Fountainbleu rock.

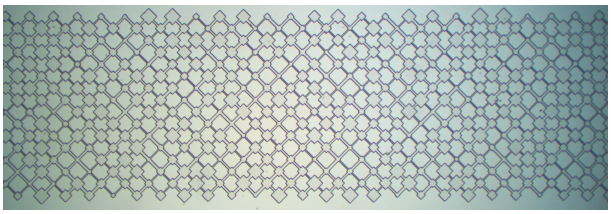

Fig. 6. A channel of a micromodel with a heterogeneous structure

Within microfluidic systems the flow is characterized by a few dimensionless numbers. The flow regime is determined by the Reynolds number (Re), which predicts whether the flow is laminar or turbulent. When Re is lower than 2,000 the flow is laminar, yet this an arbitrary number. [Squires and Quake 2005] With the microfluidic system the flow is assumed to be laminar all the time due to the small dimensions of the system. [Marre et al. 2012] Secondly there is The Peclet number (Pe) that determines the diffusion in a laminar flow. In this research project this number was not significant. Finally the Capillary number (Ca), which, as mentioned earlier, is the relationship between the viscous force and the surface tension of two fluids. Equation 1. [Squires and Quake 2005]

2. RESEARCH OBJECTIVES

In order to create an oilbank with the use of SP-flooding as EOR, different unknown questions arise, which are formulated in the research objectives below.
The outline of the paper follows the same order as the order of the research objectives. A detailed and comprehensive explanation is given of these research objective in the paper, so that the reader can fully understand the methodology that has been used, as well as the different obstacles that have been overcome.

2.1 Micromodel Experiments

The micromodel that is used for the experiments is custom designed by F.A.H Al Saadi [Al Saadi et al. 2016] and custom made by the company *Micronit*. As the micromodel has a very complex heterogeneous structure compared to older micromodel experiments, a specific set-up and protocol for these experiments had to be made. This was done to ensure that flooding of different fluids was possible within the micromodel and a full saturation was obtained. Furthermore the design of the micromodel is discussed and its shortcomings. Finally the permeability is determined experimentally as

well as theoretically, so that it can be placed in perspective to real reservoir conditions.

2.2 Formation Residual Oil

The residual oil is formed within the reservoir by the different entrapment mechanisms, and we want to see how it is formed within the micromodel. From the resulting outcome of the experiment it is then possible to analysis the data on the recovery factor with waterflooding. This is done by checking the saturation of the oil before and after the waterflooding. Also the pathway of production is checked, in order to see how fast fingering will occur within this highly complex model. These findings are then compared with the core flow experiments.

2.3 Phase Behaviour Studies

When the residual oil is formed after waterflooding, the surfactant-polymer solution will be injected in order to make the trapped oil moveable again. Therefore a phase behaviour study was done, as the displacement of multiple phases (oil-, brine- and SP-phase) is a complex phenomenon with various factors to make it successful. A microemulsion will be formed between the SP-solution and the oil phase, thereby becoming part of the fluid system, eventually leading to a change in IFT properties. This was achieved by making a series of test tubes, with changing salinity and concentration of the surfactant (Endoret O242, which is commercially manufacture by Shell). The formation time and stability of the microemulsion between the 2 phases is observed and has led to the choice of the specific surfactant-polymer solution for further experiments.

2.4 Creation of Oilbank

With the known formed residual oil within in the micromodel and the optimum surfactant-polymer solution from the phase behaviour study, the formation of an oil bank [Ng and Payatakes 1980] was attempted. The concept of an oil bank is the that the formed microemulsion propagates through the micromodel. This microemulsion bank moves through the porous medium, a bank of oil will be formed ahead of the microemulsion. The mobilized oil that at first is dispersed due to the entrapment is collected through the properties of the surfactant. The saturation of the oil bank before the emulsion bank is expected to increase over the length of the micromodel.

3. MICROMODEL EXPERIMENTS

The goal of this section is to create a protocol for the micromodel, that allows us to answer the questions posed in this study. We developed a custom made set-up, which evolved over time together with the experimental protocol until we could observe the desired dynamic processes.

3.1 Set-up

A custom designed microfluidic chip was wet etched out of silicon glass (*Micronit*, The Netherlands). [Micronit 2015] [Schlautmann et al. 2007] In the chip brine (5,000 ppm NaCl), oil (n-dodecane) and surfactant-polymer solution were injected. The micromodel was operated horizontally and therefore the gravity forces were neglected. All the experiments were done at room temperature.
The set-up for the experiment is shown below:

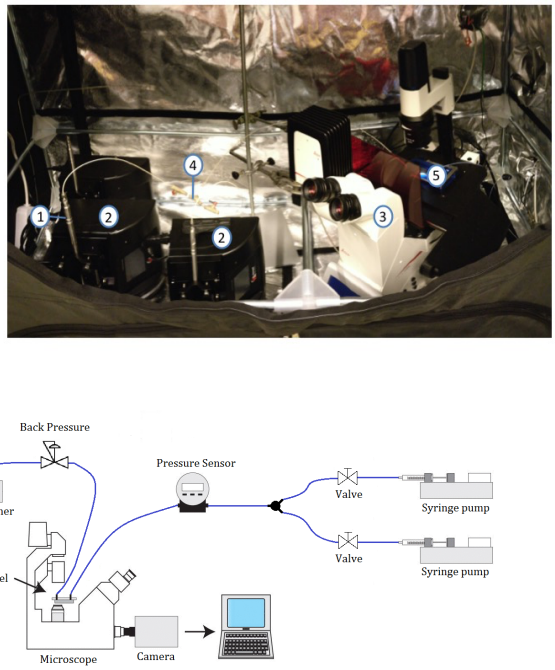

Fig. 7. Upper image displays the Set-up to conduct the experiments 1) Syringes 2) Syringe-pump 3) Microscope 4) Valves + T-junction 5) Micromodel in its holder. The lower image is a schematic representation of the set-up [Van Hoeve et al. 2011] alternation were made to represent the current set-up

The set-up consists out of 2 syringe pumps, Harvard Apparatus (Infuse/Withdraw PHD Ultra^{TM} 4400 programmable Syringe Pump). For these syringe pumps custom-made syringes stainless steel from Harvard Apparatus were used, with a volume of 8 ml. In order to measure the pressure within the system a pressure sensor was installed from General Electric, with a maximum pressure of 120 bar. Everything was connected with Peek, PolyEtherEtherKerone, tubes which have an inner diameter of 250 μm. A T-joint is installed between the two syringes pumps for optimum flow, as well as two valves to avoid the chance of back flow or pressure drop. To achieve a full saturation and to mimic core flow experiments a back pressure regulator was installed, maintaining a constant outflow pressure of 100 psi.

For capturing images on the microfluidic chip the Leica DMi8 DFC7000 microscope was used, which makes use of an inverted light microscope with transmitted light. Different objectives for magnification were used, 1.25 X and 10 X. In most cases the 1.25 objective was used so that a larger surface of the micromodel could be seen. The images were recorded with a Leica DFC7000T camera. The whole set-up was positioned within a black box, so no outside light could interfere with the light generated from the microscope.

At a certain point during the experiments 3 fluids were in the micromodel. As they were all transparent fluids, they could only be

distinguished from each other at the interface of the fluids. In order to distinguish the fluids better from each other and to obtain more valuable quantitative results a dye was added to the oil. This is Nile Red, a fluorescent solvachromatic dye, which is most notably used to dye lipid molecules due to its hydrophobicity [Brujić et al. 2007]. Fluorescence is the emission of light by a material when it is excited by a wavelength within a specific range (the excitation spectrum). The Nile Red gives a fluorescence red glow at a wavelength between 559 - 637nm. [Greenspan et al. 1985][Datta et al. 1997]

3.2 Protocol for experiments

In the beginning the experiments were running unsatisfactory. When only brine was injected, pockets of gas were still in the system after breakthrough. This could be resolved by two additions to the experiment setup. Firstly a back pressure regulator was added to avoid the formation of gasses during the experiments. Secondly CO_2 was injected in the micromodel prior to the injection of the brine. CO_2 replaces the air in the micromodel. Subsequently the CO_2 dissolves in the brine and is displaced from the micromodel through the brine phase. Without CO_2 injection the risk exists that air gets capillary trapped in the micromodel, adding another phase in the micromodel, which we try to avoid. These two additions to the micromodel allow 100% saturation with oil and brine of the micromodel.

Running Experiments

(1) *Turn on the camera*
Now it is possible to gather images during the experiments

(2) *Inject CO_2 in the system for 15 min at a pressure of 8 - 10bar*
CO_2 can be dissolved in the brine. Thanks to this feature it is possible to reach 100% saturation in the microchip.

(3) *Start injection of Brine*
An injection speed of 0.1 μl/min and a total of 10 times the pore volume has to be inject in the micromodel.

(4) *Start injection of dyed Dodecane*
When starting the injection, remember that first all the brine in the tubing has to pass through the set-up before the oil can reach the microchip inlet. The injection speed remains 0.1 μl/min and a total of 10 times the pore volume has to be inject in the micromodel. At this point a reservoir condition is mimicked

(5) *Start actual experiment waterflooding*
Start injection brine in order to mimic waterflooding. The injection speed should be set at reservoir condition, 1 ft a day. The total length of the microchip is 79 cm = 2.59 ft, so it should take 2.6 days to go through the chip. With a pore volume of 18 μl it means that an injection speed of 0.29 μl/hour or 4.8 nl/min is required. This is not possible using the syringe pump that was available. An injection speed of 0.1 μl/min was therefore used in these experiments.

(6) *Start injection of surfactant*
Start injection of the surfactant at the same speed as the waterflooding was done

The complete protocol, including operational protocol, start-up experiments and cleaning protocol, is described in Appendix B.

3.3 Micromodel

As mentioned the micromodel is based on the properties of the fountainblue rock. [Al Saadi et al. 2016] The specific design features can be found in Appendix C.

During the experiments it became clear that the micromodel did not meet the requirements and that it had to be redesigned. The reason behind this was that occasionally clogging occurred at the inlet/outlet point of the micromodel. At first instance, it was tried to wash away the clogging from the inlet/outlet point by reversing the fluid flow in the micromodel. Unfortunately, this was not successful. The pressure in the micromodel increased so much when reversing the flow, that the tube on the micromodel loosened. The cause for this was that the micromodel holder did not sufficiently fix the tube when the pressure exceeded 15 bars. Once the tube loosened the pressure in the micromodel disappeared, making it impossible to wash the clogging away at the inlet/outlet point. In order to deal with this problem the micromodel was redesigned by adding a filtration system within the inlet of the micromodel. This can be seen in Figure 8. Furthermore a new fixation system with screws instead of rubber clamps for the tubing on the micromodel was designed. This redesign should avoid clogging of the inlet/outlet point as well as allow for experiments at a pressure above 15 bar. A picture of the old and new micromodel holder can be found in Appendix C.

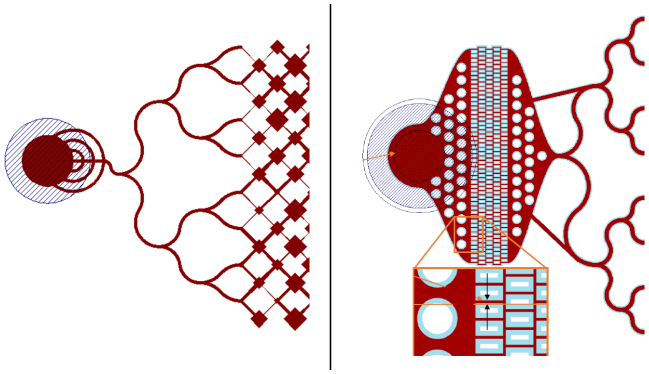

Fig. 8. On the left the initial design of the inlet. On the right the new design with the filtration system in it

For future experiments the new design can be used and with the addition of the customized protocols, experiments will run probably run more smoothly. Yet the cleaning is still an issue, as *Micronit* designed these micromodels to retain the fluids in the chip. Drying is a possibility, however, if there is still brine in the system after the cleaning protocol, salt crystals will be formed. On this matter it is recommended to store micromodel in a container filled with demiwater and immerse it, so that no formation of salt or any mineral can occur.

3.4 Permeability calculations

With the specific design of our micromodel the permeability was unknown, and had to be calculated theoretically as well as experimentally. The theoretical permeability can be calculated through the parallel plate model. The different pore sizes of the micromodel were set in a string with a pore throat in between. Where the pore throat is the harmonic average of the 4 different throats.

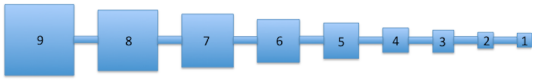

Fig. 9. 9 different pore sizes with the harmonic average of the pore throat in between

These pores and throats are than represented as the void space between two parallel plates. The flow between the plates is assumed to be steady state and laminar incompressible flow, this gives an exact solution for the Stokes equation:

$$\mathbf{Q} = \frac{\mathbf{wh^3}}{\mathbf{12}\mu}\left(\frac{\mathbf{\Delta P}}{\mathbf{L}}\right) \tag{3}$$

When substituting the volumetric flow rate, Q, by the Darcys law Equation 5, an expression for parallel plate permeability (k) in unit lengths is obtained as $wh = A$:

$$\mathbf{k} = \frac{\mathbf{h^2}}{\mathbf{12}} \tag{4}$$

The permeability of each pore cell can be found in the table in Appendix C. The harmonic average pore throat is $8.90E-12m^2$, which is located between each pore cell. The overall theoretical harmonic permeability was determined as $1.90E-11m^2$ or $19,251mD$.
The experimental permeability was calculated through Darcy's law which is given express in equation below.

$$\mathbf{Q} = \frac{\mathbf{kA}}{\mu}\frac{\mathbf{\Delta P}}{\mathbf{L}} \tag{5}$$

Reformulation of Darcy's law gives the following equation of the permeability,

$$\mathbf{k} = \frac{\mathbf{QL}}{\mathbf{A}}\frac{\mu}{\mathbf{\Delta}} \tag{6}$$

The following parameters were used: $Q = 0.1\mu l/min = 1.66E-09kg/s$, the flowrate in the microchip; $A = 0.003m$, cross-section of the channel; $L = 0.79m$, length of the chip, $\mu = 1.011cp = 0.001011Pa.s$ the viscosity of the fluid (brine of 5000ppm). For ΔP an assumption was made. The inlet pressure is the same as the pressure given by the pressure sensor and the outlet pressure is the same as the back-pressure, in this case $100PSI$. The inlet pressure is averaged over a hour and was $9.2bar$. This gives an ΔP of $2.7bar$ Thus the experimental permeability is equal to $1.115E-13m^2$ or $112.9mD$

The difference in these two permeabilities is a factor 10, the difference is due to some shortcomings on using the parallel plate method. At first all pores are assumed to go in the same direction. Secondly the string model is an oversimplification of the porous media. At last tortuosity is not considered.

3.5 Image analysis

The outcome of the experiments are images which were analysed using ImageJ software. Two types of images were recorded: colored images with fluorescent light and grayscale images with regular transmitted light. The fluorescent images contain the information that enables ImageJ to differentiate between fluids in the system. The fluorescent light does not highlight the pore structure as it only capture the fluorescence. The regular bright light images are used in combination with the fluorescent images to highlight the pores of the micromodel. Images were taken at a pre-set location on the micromodel, allowing an accurate comparison during the experiments.

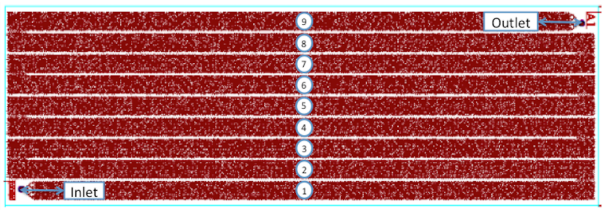

Fig. 10. Micromodel with the preset location for capturing images

4. FORMATION OF RESIDUAL OIL

During this research project the formation of residual oil was studied, according to the protocol described in appendix B. Firstly the oil saturation of the micromodel was studied and calculated. Secondly the micromodel was water flooded and the oil saturation was recalculated and the recovery factor was determined. Also an attempt was made to understand the entrapment mechanism in the micromodel. These results were then compared with coreflow experiments done prior to this research project.

4.1 Oil saturation in micromodel

The saturation was calculated by measuring the oil volume in comparison to the pore network volume. The oil is highlighted in red in the fluorescence image due to the presence of the Nile Red. The pore network is viewed in a bright-light image. In figure 11 the saturation on position 9 is displayed with the corresponding pore network of the micromodel.

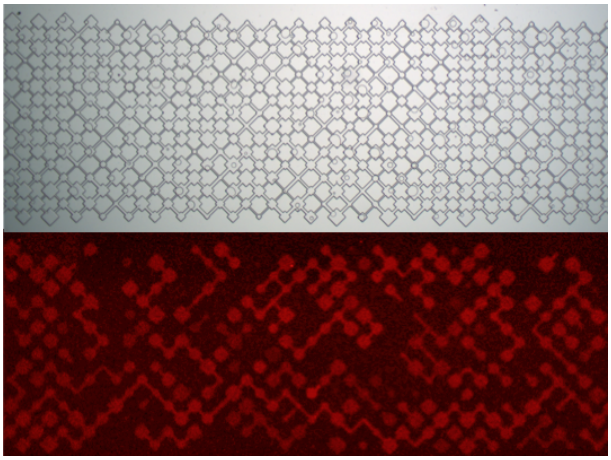

Fig. 11. Corresponding images of position 9, with the upper image displaying the pore network in bright-light. The lower image displays the oil saturation in that specific pore network

These images have been analyzed by ImageJ Software. The result can be found in figure 12. The total area of the pore-network model is $17.93mm^2$ and fluorescence oil within the pore network has an

area of $10.95mm^2$. This gives an overall saturation of 61.1% in the micromodel on position 9.

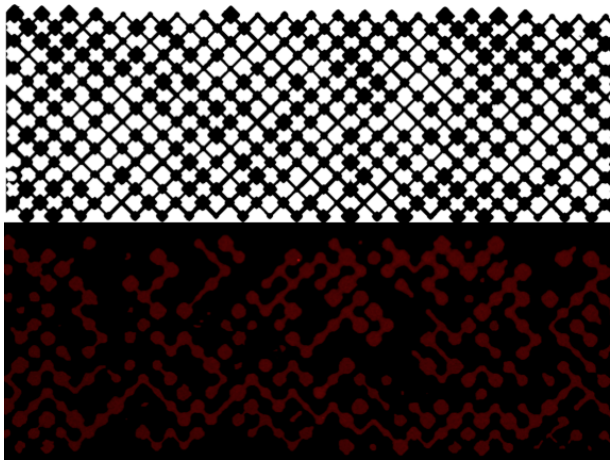

Fig. 12. Upper image displays the the pore network after processing through ImageJ. The lower image the oil saturation after processing through ImageJ

In order to find the saturation over the whole micromodel the saturation was calculated over the different positions on the micromodel. Due to low image quality on position 1 through 4, these were left out from the analysis. In table I an overview is displayed of each position with its specific saturation. The corresponding microscopic images for the different positions can be found in Appendix D

Table I. Oil saturation before waterflooding over the different positions

Channel number	Area porenetwork $[mm^2]$	Area oil $[mm^2]$	Saturation $[\%]$
9	10.5	6.4	61.1
8	11.2	6.4	57.4
7	10.9	6.3	58.2
6	10.1	6.1	60.2
5	9.9	5.4	54.4

The average saturation of the different positions is 58.3% with a standard deviation of 6%. This value is assumed to be the saturation level of the micromodel and has been used for further analysis.

4.2 Oil saturation after waterflooding

Again multiple pictures were taken from the micromodel and the residual oil saturation was calculated through ImageJ Software. In figure 13, the oil saturation is displayed before and after waterflooding of channel 9.

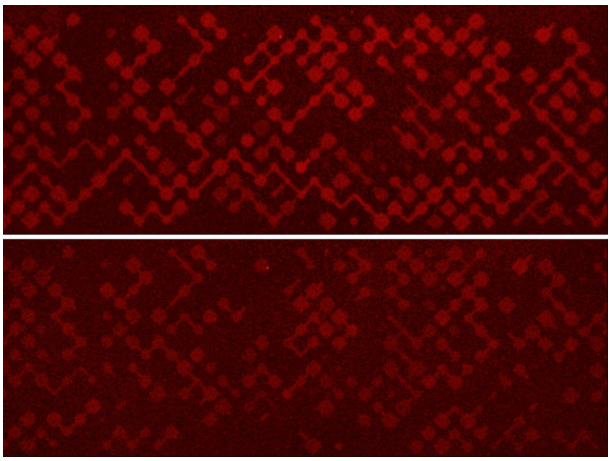

Fig. 13. Upper image displays the saturation of oil before WF and the lower image the saturation of oil after WF

From the analysis it can be determined that the saturation of position 9 after waterflooding is 48.0% compared to the initial oil saturation of 61.1%. This gives a recovery factor of 21.4% The overall recovery factor is determined by averaging the different positions on the micromodel. Therefore the residual oil saturation of the different positions needs to be known, as is displayed in table II. The corresponding microscopic images can be found in Appendix D

Table II. Oil saturation after waterflooding over the different positions

Channel number	Area porenetwork $[mm^2]$	Area oil $[mm^2]$	Saturation $[\%]$
9	10.9	5.2	48.0
8	8.6	3.9	45.8
7	10.1	4.0	39.5
6	9.5	4.6	48.5
5	10.1	3.9	38.8

The average saturation after waterflooding of the different positions is 44.2% with a standard deviation of 4.6%.From table I & II the recovery can be calculated of each channel, this is given in table III

Table III. Recovery over the different positions

Channel number	Saturation before WF $[\%]$	Saturation after WF $[\%]$	Recovery $[\%]$
9	61.1	48.0	21.4
8	57.4	45.8	20.2
7	58.2	39.6	32.0
6	60.2	48.5	19.3
5	54.4	38.8	28.6

The average saturation after waterflooding of the different positions is 58.3% with a standard deviation of 2.6%. The average recovery is 24.3% with a standard deviation of 5.6%. These values are assumed to be the saturation and recovery level of the micromodel and have been used for further analysis.

4.3 Comparison to coreflow experiments

Previous core-flow experiments have been conducted with a core from the Fontainebleau rock. Here an oil saturation of 70% has been realized with a recovery factor of 30%. It can be concluded that the design of the pore network in the micromodel is satisfactory. Besides the standard deviation, there is also a margin of error in the image analyses. It proofs that the conclusion and observation within the micromodel can be applied on core flow experiments.

5. ANALYSIS OF RESIDUAL OIL

In this section the formed residual oil is analyzed. This results in a close look at the oil ganglion size before and after waterflooding, as well as the size distribution over the different positions. All this leads to a conclusion about the entrapment within the micromodel.

5.1 Oil ganglion size distribution

With the images that were obtained from the analyses of the saturation and the recovery, an analysis of the oil ganglia was made. At first an analysis of the total distribution was made followed by a more detailed analysis of the distribution of the smaller oil ganglia. This ensures a better visualization of the oil ganglion changes after waterflooding in the micromodel. A cumulative curve was made of the oil ganglion sizes, delivering a similar recovery factor for each position as in section of oil saturation. The detailed analysis of position 9 in the micromodel is shown below. The results of the other positions are displayed in table IV. The analysis for the oil ganglia was made using ImageJ software. The image in figure 14 shows the oil ganglion sizes before and after waterflooding. Due to the image processing by ImageJ, noise-particles appeared in the micromodel, but these were discarded for the analysis.

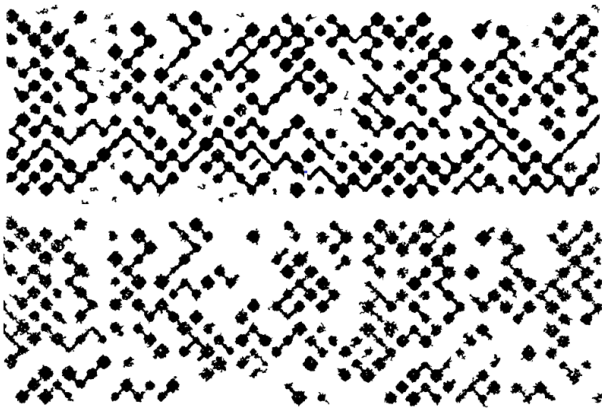

Fig. 14. Oil ganglion network on position 9. The top network is before waterflooding, bottom is after waterflooding.

From each image of figure 14 the size of the oil ganglia was determined. The results were plotted in a histogram displaying the entire distribution of oil ganglion sizes, as can be seen in figure 15.

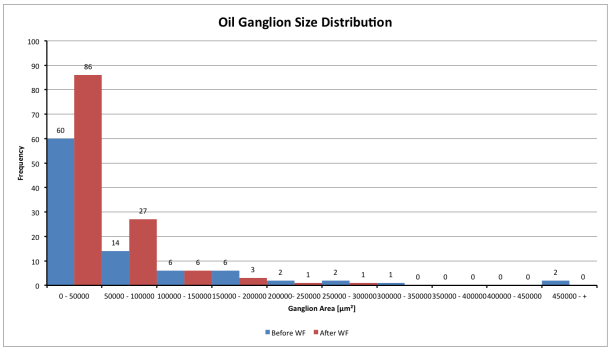

Fig. 15. Histogram of the oil ganglion size distribution.

To have all the data plotted in the histogram a wide bin range had to be used. Nevertheless it is clear to see that the frequency of small oil ganglia is greater after waterflooding, and that the oil ganglia found in the latest bin before waterflooding have disappeared. These findings are also visually confirmed when looking at the network pattern in figure 14.

A new more detailed histogram with narrower ranges was made to plot the small oil ganglia. This gives a better inside in the small oil ganglia frequency and the understanding of the entrapment.

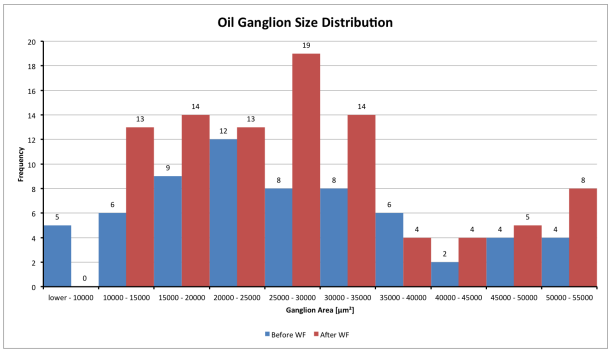

Fig. 16. Histogram of the oil ganglion size distribution, with a maximum size of $50,000 \mu m^2$

In figure 16 a clear change in the frequency of oil ganglion sizes can be seen. The smallest range has disappeared. This could be due to the image analysis, but also due to the clustering of oil ganglia. For the other ranges it is apparent that the frequency of small oil ganglia becomes greater after waterflooding, which is seen over all the positions.

By comparing a cumulative distribution of the oil ganglion size before and after waterflooding, it is possible to determine the recovery. The graph displays the overall area of initial oil and the area of oil left after waterflooding.

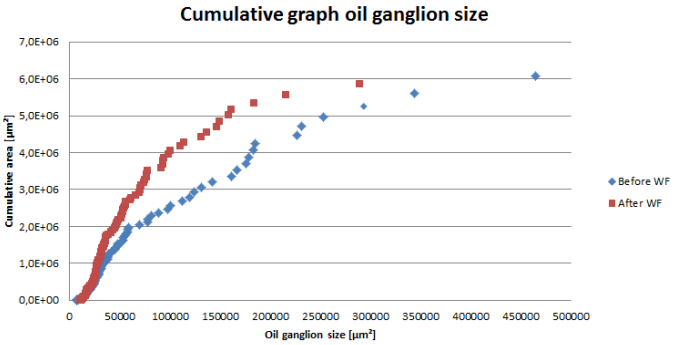

Fig. 17. Cumulative curve of the oil ganglion size before and after waterflooding for position 9. Note: the last oil ganglion is not on the graph, now the gap is clearer

In figure 17 a clear gap between the cumulative curves for position 9 is seen. This shows that there is an increase in smaller oil ganglia. The total cumulative area is $7.64mm^2$ before waterflooding and $5.87mm^2$ after waterflooding, giving a recovery of 23.4%. For the other positions on the micromodel similar cumulative graphs were made, which can be found in Appendix D. The corresponding recovery factor for each position is given in table IV, where the recovery results previously generated in table III are compared with the results in this section.

Table IV. Recovery over the different positions

Channel number	Recovery Image analysis [%]	Recovery Oil ganglion analysis [%]
9	21.4	23.4
8	20.2	24.2
7	32.0	26.3
6	19.3	22.7
5	28.6	24.3

There is some offset between the two recovery numbers, the different methods has both a flaw in their procedure. A sensitivity analysis has to be made to see which method is the most valid.

5.2 Analysis of entrapment

It was not possible to capture any snap-off mechanism, due to the fact that the shutter time for making fluorescence images was one second, which is too long. Nevertheless it is believed that the main trapping mechanism is bypassing, as can be clearly seen in figure 19 when the waterfront is fingering through the network during waterflooding.
This proves that the waterfront follows the path of least resistance in the micromodel. However, one has to realize that these are snapshots of the waterflooding. When looking at figure 18 the pathway of the waterfront is clearly visible, but the figures also show other places of bypassing. When snap-off occurs it mainly leaves an oil droplet in the micromodel as can be seen in figure 18. These droplets were formed out of an initial oil ganglion. Still this is an assumption as there are no valid data to support this. From figure 18 it can be concluded that the main mechanism for the entrapment of residual oil is by-passing, which corresponds with previous literature [Morrow et al. 1988].

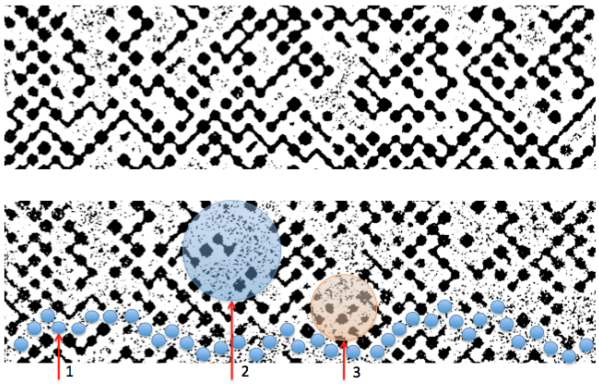

Fig. 18. The upper image shows the initial saturation. The lower image shows the formed residual oil where 3 entrapment section are highlighted 1) the pathway of the waterflooding 2) area where bypassing has occurred 3) possible snap-off droplets

5.3 Velocity of oil ganglia

During the waterflooding experiment, multiple video clips were made. In these clips one can observe the waterfront propagating through the micromodel. Knowing the size of scale in the clips, the speed of the waterfront could be determined. In figure 19 the propagation of the waterfront at time intervals $t = 0s$ and $t = 20s$ is shown. From these images the velocity of propagation of the waterfront in the x-direction was calculated, being $270\mu m/s$.

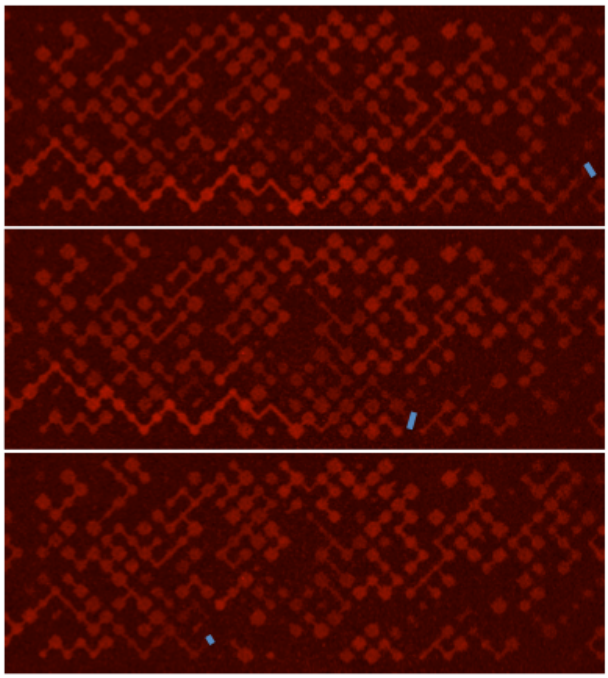

Fig. 19. The propagation of the Waterfront is displaced with the blue line, with the upper image at time = 0 s, the middle at time = 10 s and the lower image at time = 19 s

With the help of the same video clip, a similar analysis was made of the propagation of two oil ganglia. The analysis showed that the oil ganglia with the smaller size goes at higher velocity through the micromodel compared to the oil ganglia with the larger size, see table V. The specific image sequence over time of the two oil ganglia can be found in the appendix D

Table V. Velocity waterfront & oil ganglia

	velocity $[\mu m/s]$	ganglia size $[mm^2]$
Waterfront	270	-
Oil ganglia 1	298	0.187
Oil ganglia 2	288	0.235

It is not possible to draw statistically significant conclusions from these three velocity analyses. More data will have to be gathered to allow analyses on a broader range of oil ganglia sizes, in order to investigate a possible correlation between velocity and size.

6. SURFACTANT BEHAVIOUR

To establish a better displacement of the residual oil a surfactant-polymer mix was made. The perfect concentration of the surfactant-polymer had to be determined along two parameters: the salt (NaCl) concentration and the SBA (2-butanol) concentration, a co-solvent. It is expected that a higher co-solvent facilitates a better microemulsion formation.[Barnes et al. 2010] The surfactant-polymer solution that varies in salinity and SBA concentration is prepared in a test tube of 20ml, and consist of 10 ml of the surfactant-polymer solution and 10 ml of dodecane (mixing ration of 1:1). The test tubes were shaken vigorously and then the tubes were put to rest for 24h, allowing the oil and water phase to separate. Between the two phases a clear microemulsion was formed which contained most of the surfactant with some dodecane and brine.

Firstly the ideal salt concentration was determined with only surfactant in solution (0.5% w/w of Endoret O242). A range was made from 2 - 5% (w/w) of salt in the surfactant solution. The resulting microemulsion are shown in the picture below. From these picture there is a clear turning point between 2% and 4%(w/w) salt concentration. The main difference between these concentrations is the amount of microemulsion formed between the oil and aqueous phase within the test tubes. For that reason a more detailed experiment was carried out with concentrations that vary between 2 - 4% and increment with 0.5% The results can be found in the picture below.

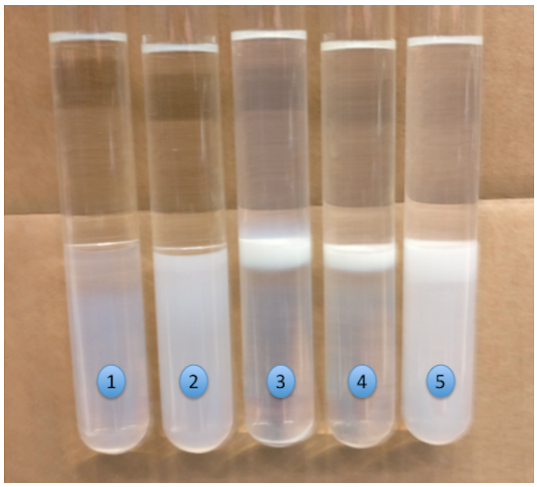

Fig. 20. Phase behaviour test (0.5% w/w O242 and 1% SBA) with different NaCl concentration; 1) 2%, 2) 2.5%, 3) 3%, 4) 3.5%, 5) 4%

From figure 20 it is clear that an optimum is reached around a salt concentration of 3.5% (w/w), when a significant microemulsion is visible in the test tubes. The concentration of the surfactant polymer in the salt solution of this experiment was 1% (w/w) SBA.
A similar range of salt solution was made with a SBA concentration of 4%. As can be seen from the resulting picture a more stable microemulsion with a better interface is obtained with a salt concentration of 4% (w/w) and a SBA concentration of 4%.

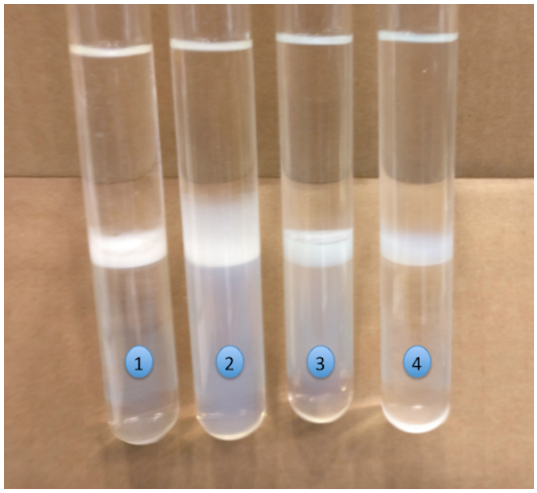

Fig. 21. phase behaviour test (0.5% w/w O242 and 4% SBA) with different NaCl concentration; 1) 2%, 2) 3%, 3) 3.5%, 4) 4%,

From this phase behaviour the surfactant-polymer mixture with the best looking microemulsion was chosen, i.e. a 4% SBA concentration and a 4% NaCl concentration. At these concentrations the best displacement of the residual oil was expected.

7. CREATION OF OILBANK

At this point of the research project the injection of the surfactant-polymer solution in the system occurred. It is of great interest to capture the mobilization of the residual oil forming a new oil bank.

7.1 Oilbank Creation due to Surfactant-Polymer Flooding

After the analysis of the phase behaviour, the injection of the SP solution took place. A problem occurred when the SP solution reached the inlet of the micromodel. Due to the white appearance of the white microemulsion and SP solution, the UV-light reflected red on the images, making it nearly impossible to distinguish the oil from the SP solution.

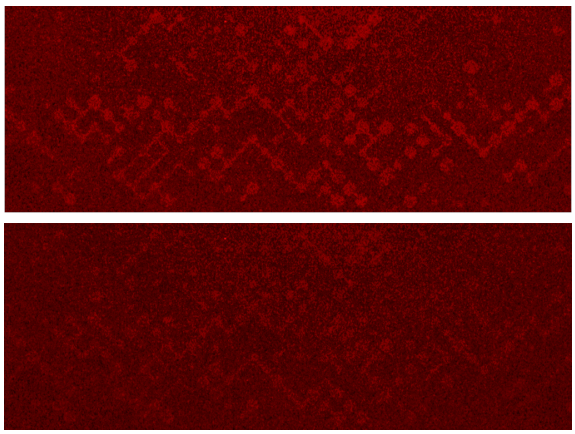

Fig. 22. The upper image displays the residual oil. The lower images displays the propagation of the surfactant. It becomes harder to distinguish the different phases

As such there appears to be a continuous stream of the fluorescent oil, see figure 23, although it is known that this is not possible due to the fact there is still a stream of oil after injection of 3 times pore volume of the SP flooding. This indicates the problem of the reflection of the white SP solution.

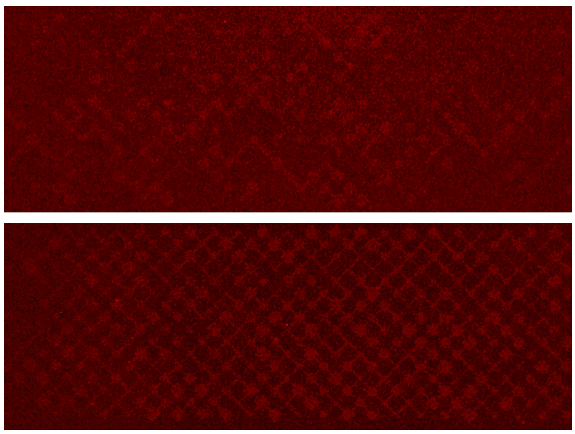

Fig. 23. The upper image displays the residual oil being "moved out". The lower images displays the propagation of the SP solution where it becomes a clear red phase.

A bright-light image sequence was made whether a change in the micromodel could be visualized, as shown in figure 24. When comparing the image taken on position 2 and position 9 there is a change in what appear to be oil droplets. On position 2 the numbers of "oil droplets" is less than on position 9. This possible can be explained by the fact that the surfactant only gets oil droplets partially out of the residual oil.

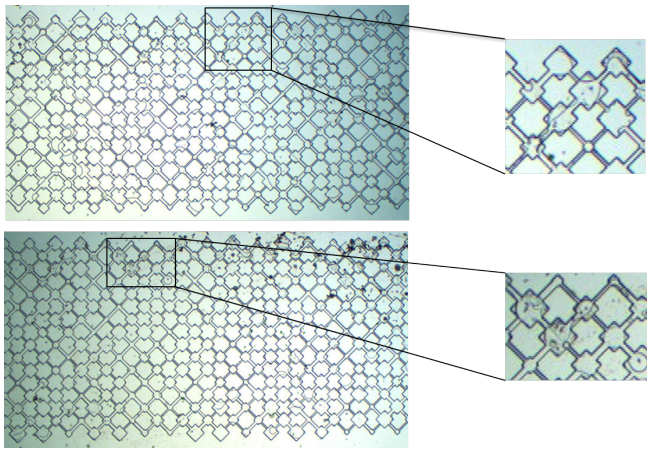

Fig. 24. The upper image displays position 2 where the surfactant flows at the top with almost none oil droplets. The lower image displays position 9 where the surfactant flows at the top with a higher concentration of oil droplets.

This means that the full recovery of residual oil requires multiple pore volumes of surfactant which is not practically in oil fields. The required amount of surfactant is just too high to make it economically attractive. A possible solution lies in increasing the viscosity of the SP-flooding, which is done by increasing the polymer concentration. Unfortunately it is not possible to quantify the figure as there is no possible distinguish of the different phases.

The surfactant fingered through the micromodel as was seen in figure 24. Similar results were found with previous conducted core-flow experiments when only surfactant solution was injected. This can be found in figure 25. It shows the propagation of the surfactant in a core flow, were a clear fingering occurs.

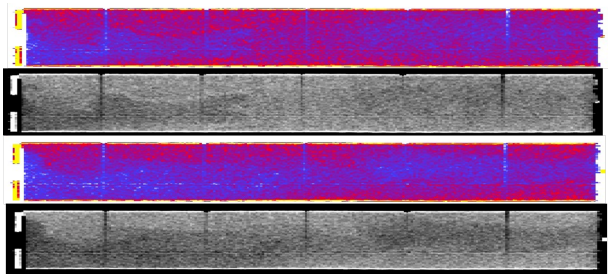

Fig. 25. Displays core flow experiments with a color and a grayscale image. The upper two images displays the movement of the surfactant. The lower two images shows the surfactant pathway at break through

8. DISCUSSION AND RECOMMENDATIONS

- The injection rate should be lower, but due to the limit of the diameter of the syringe this was not possible. With an injection rate of $0.1\mu l/min$, a total volume of $18\mu l$ and a length of $0.79m$ the front would move $6.32m/day$ or $20.73ft/day$ where normal oil field would have a rate of $1ft/day$. To fully understand the mechanism a lower injection rate is required, therefore a syringe with smaller diameter is needed. Hence the duration of the experiments will take longer.
- The achieved recovery factor and different oil saturations are satisfactory and comparable with those of previous coreflow experiments. Yet the injection rates of the experiments are different. In order to obtain comparable data and better conclusions, similar experimental conditions should be applied.
- The entrapment of residual oil is mainly formed due to bypassing. This was seen with the waterfront propagation during waterflooding. A clear snap-off was not captured, as the angle of the camera was too wide and the resolution time was too long. In order to capture the snap-off mechanism an objective with a larger magnification should be used. The Jamin-effect could not clearly be observed.
- It was a problem to determine the creation of an oilbank as the oilbank could not be visualize due to the reflection of the SP-solution. Instead of working with a fluorescence dye under UV-light, a dye that is visible in bright-light should be used. This allows a sharper and clearer capturing of images, making the analysis more accurate.
- The addition of a co-solvent has a positive influence on the formation of the microemulsion. When applying a lower injection rate of the SP-solution, the formation time for the microemulsion increases, thereby increasing the microemulsion volume and thus a better displacement can be achieved.
- The micromodel gives a detailed understanding of the change in oil ganglia sizes after waterflooding, and the opportunity to determine the velocity of oil ganglia during waterflooding. More research needs to be done in order to draw solid conclusions.

9. CONCLUSION

- The set-up of the micromodel and the protocol for conducting for the experiments are suitable for future research projects. It can contribute to the development of new EOR technique. The micromodel allows visualization of the dynamic fluid processes and flow-regimes. Due to the longer pathway and greater heterogeneity of the micromodel, a better mimicking of coreflow experiments is possible.
- A new micromodel inlet and micromodel chipholder was designed. This allows to work with higher pressure due to the better connections on the in/outlet. The build in filtration system ensures that no clogging can occur in the micromodel.
- Compared to previously conducted coreflow experiments, similar results for oil saturation and recovery were realized.
- The selected SP-solution forms a clear and sharp microemulsion layer between the oil phase and the SP phase. The SP-solution consists of 0.5 % w/w of Endoret-O242 surfactant, 150ppm of HPAAM-3630 polymer, 4 % co-solvent (SBA) and has a salinity of 4 %. It is suitable for future experiments.
- The attempt to create an oilbank was unfortunately not successful. UV-light does not allow for discrimination between SP-solution and the Red-Nile dyed oil, required to visualize the oilbank.

ACKNOWLEDGMENTS

I am grateful to the following people for resources, constructive discussions and valuable suggestions: Prof. Ir. C.P.J.W. van Kruijsdijk (TU Delft), Msc. F.S.H. Al Saadi (TU Delft and Dr. K.H.A.A. Wolf (TU Delft). And special mention to M. Slob and J.G. van Meel, those who helped me extensively in the laboratory.

NOMENCLATURE

List of Symbols

N_c	=	Capillary number
μ	=	Viscosity
σ	=	Surface tension
v	=	Superficial tension
P_c	=	Capillary pressure
w	=	Width
k	=	Permeability
h	=	Height
Q	=	Flow rate
A	=	Surface
ΔP	=	Pressure difference
L	=	Length
P	=	Pressure
q	=	Volume flowrate
D	=	Diameter
Θ	=	Contact angle
R	=	Radius

Subscripts

w	=	wetting phase
nw	=	non-wetting phase
wi	=	wetting phase at the interface
nwi	=	non-wetting phase at the interface
ow	=	interface oil & water

REFERENCES

A.Z. Abidin, T. Puspasari, and W.A. Nugroho. 2012. Polymers for enhanced oil recovery technology. *Procedia Chemistry* 4 (2012), 11–16.

A. Abrams and others. 1975. The influence of fluid viscosity, interfacial tension, and flow velocity on residual oil saturation left by waterflood. *Society of Petroleum Engineers Journal* 15, 05 (1975), 437–447.

M.S. Al-Gharbi and M.J. Blunt. 2005. Dynamic network modeling of two-phase drainage in porous media. *Physical Review E* 71, 1 (2005), 016308.

F.S.H. Al Saadi and others. 2016. A Revised Workflow for Spatial and Petrophysical Rock Characterization: The Fontainebleau Case. In *NAC: Nederlands Aardwetenschappelijk Congres*. Utrecht, The Netherlands. https://nacgeo.nl/conference-details/programme/poster/691

J.R. Barnes, H. Dirkzwager, J. Smit, J. Smit, A. On, R.C. Navarrete, B. Ellison, M.A. Buijse, and others. 2010. Application of internal olefin sulfonates and other surfactants to EOR. Part 1: Structure-Performance relationships for selection at different reservoir conditions. In *SPE Improved Oil Recovery Symposium*. Society of Petroleum Engineers.

J. Brujić, C. Song, P. Wang, C. Briscoe, G. Marty, and H.A. Makse. 2007. Measuring the coordination number and entropy of a 3d

jammed emulsion packing by confocal microscopy. *Physical review letters* 98, 24 (2007), 248001.

I. Chatzis and F.A.L. Dullien. 1983. Dynamic immiscible displacement mechanisms in pore doublets: theory versus experiment. *Journal of Colloid and Interface Science* 91, 1 (1983), 199–222.

I. Chatzis, N.R. Morrow, and others. 1984. Correlation of capillary number relationships for sandstone. *Society of Petroleum Engineers Journal* 24, 05 (1984), 555–562.

National Petroleum Council and National Petroleum Council. Committee on Enhanced Recovery Techniques. 1976. *Enhanced oil recovery, EOR: an analysis of the potential for enhanced oil recovery from known fields in the United States, 1976 to 2000*. National Petroleum Council.

A. Datta, D. Mandal, S.K. Pal, and K. Bhattacharyya. 1997. Intramolecular charge transfer processes in confined systems. Nile red in reverse micelles. *The Journal of Physical Chemistry B* 101, 49 (1997), 10221–10225.

W.B. Gogarty and others. 1967. Mobility control with polymer solutions. *Society of Petroleum Engineers Journal* 7, 02 (1967), 161–173.

P. Greenspan, E.P. Mayer, and S.D. Fowler. 1985. Nile red: a selective fluorescent stain for intracellular lipid droplets. *The Journal of cell biology* 100, 3 (1985), 965–973.

M.J. Jamin. 1860. On the equilibrium and motion of liquids in porous bodies. *The London, Edinburgh, and Dublin Philosophical Magazine and Journal of Science* 19, 126 (1860), 204–207.

W.G. Laidlaw and N.C. Wardlaw. 1983. A theoretical and experimental investigation of trapping in pore doublets. *The Canadian Journal of Chemical Engineering* 61, 5 (1983), 719–727.

R. Lenormand, C. Zarcone, and others. 1984. Role of roughness and edges during imbibition in square capillaries. In *SPE annual technical conference and exhibition*. Society of Petroleum Engineers.

R. Lenormand, C. Zarcone, and A Sarr. 1983. Mechanisms of the displacement of one fluid by another in a network of capillary ducts. *Journal of Fluid Mechanics* 135 (1983), 337–353.

D. Levitt, A. Jackson, C. Heinson, L.N. Britton, T. Malik, V. Dwarakanath, G.A. Pope, and others. 2006. Identification and evaluation of high-performance EOR surfactants. In *SPE/DOE Symposium on Improved Oil Recovery*. Society of Petroleum Engineers.

S. Marre, Y. Roig, and C. Aymonier. 2012. Supercritical microfluidics: Opportunities in flow-through chemistry and materials science. *The Journal of Supercritical Fluids* 66 (2012), 251–264.

C.D. McAuliffe and others. 1973. Oil-in-water emulsions and their flow properties in porous media. *Journal of petroleum technology* 25, 06 (1973), 727–733.

Micronit. 2015. Wet Etching. (2015). http://www.micronit.com/technologies/fabrication-technologies/etching/

T.F. Moore and R.L. Slobod. 1956. The effect of viscosity and capillarity on the displacement of oil by water. *Producers Monthly* 20, 10 (1956), 20–30.

N.R. Morrow, I. Chatzis, J.J. Taber, and others. 1988. Entrapment and mobilization of residual oil in bead packs. *SPE Reservoir Engineering* 3, 03 (1988), 927–934.

N. Mungan, F.W. Smith, J.L. Thompson, and others. 1966. Some aspects of polymer floods. *Journal of Petroleum Technology* 18, 09 (1966), 1–143.

K.M. Ng and A.C. Payatakes. 1980. Stochastic simulation of the motion, breakup and stranding of oil ganglia in water-wet granular porous media during immiscible displacement. *AIChE Journal* 26, 3 (1980), 419–429.

PERM-Inc. 2013. Fundamentals of Fluid Flow in Porous Media. (2013). http://perminc.com/resources/fundamentals-of-fluid-flow-in-porous-media

J.G. Roof and others. 1970. Snap-off of oil droplets in water-wet pores. *Society of Petroleum Engineers Journal* 10, 01 (1970), 85–90.

S. Schlautmann, A. Van den Berg, and J.G. Gardeniers. 2007. Microfluidic device. (Aug. 22 2007). US Patent App. 11/843,124.

D.O. Shah. 1981. *Surface phenomena in enhanced oil recovery*. Springer.

D.O. Shah. 2012. *Improved oil recovery by surfactant and polymer flooding*. Elsevier.

Shell-Chemicals. 2015. Enordet: Detergents for Enhanced Oil Recovery. (2015). http://www.shell.com/business-customers/chemicals/our-products/higher-olefins-and-derivatives/enordet-surfactants

W.O. Smith and M.D. Crane. 1930. The Jamin effect in cylindrical tubes. *Journal of the American Chemical Society* 52, 4 (1930), 1345–1349.

T.M. Squires and S.R. Quake. 2005. Microfluidics: Fluid physics at the nanoliter scale. *Reviews of modern physics* 77, 3 (2005), 977.

G.L. Stegemeier. 1977. Mechanisms of entrapment and mobilization of oil in porous media. *Improved Oil Recovery by Surfactant and Polymer Flooding* (1977), 55–91.

G.J. Stosur and others. 2003. EOR: Past, present and what the next 25 years may bring. In *SPE International Improved Oil Recovery Conference in Asia Pacific*. Society of Petroleum Engineers.

J.J. Taber and others. 1969. Dynamic and static forces required to remove a discontinuous oil phase from porous media containing both oil and water. *Society of Petroleum Engineers Journal* 9, 01 (1969), 3–12.

S. Thomas, S.M. Ali, and others. 1999. Micellar flooding and ASP-chemical methods for enhanced oil recovery. In *Annual Technical Meeting*. Petroleum Society of Canada.

L.C. Uren, E.H. Fahmy, and others. 1927. Factors influencing the recovery of petroleum from unconsolidated sands by waterflooding. *Transactions of the AIME* 77, 01 (1927), 318–335.

W. Van Hoeve, B. Dollet, M. Versluis, and D. Lohse. 2011. Microbubble formation and pinch-off scaling exponent in flow-focusing devices. *Physics of Fluids* 23, 9 (2011), 092001.

APPENDIX

A. APPENDIX A

Bypassing

The condition that bypassing happens in the larger pore during the imbibition could be found by using the capillary and viscous forces formula. In order get govern equation the pore doublet model from Chatzis et al. is used and shown in figure 26. [Chatzis and Dullien 1983]

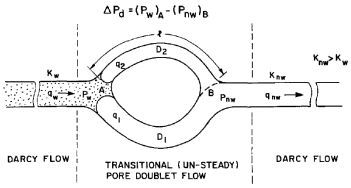

Fig. 26. Conventional pore doublet model representation of imbibition, flow rate goes to the right. [Chatzis and Dullien 1983]

If water is supplied at the volume flowrate of $\mathbf{q_w}$ to the doublet then $\mathbf{q_1} + \mathbf{q_2} = \mathbf{q_w}$ where $\mathbf{q_1}$ and $\mathbf{q_2}$ are the flow rates in the two channels. The assumption was made that when the fluid-fluid interaction was establish in one of the channel, it would advance simultaneously and the viscous pressure drops. The magnitude of the viscous pressure drops were assumed to be given by the Hagen-Poiseuille equation:

$$\mathbf{\Delta P_j} = \frac{\mathbf{128 q_j \mu l}}{\pi \mathbf{D_j^4}} \tag{7}$$

Where j = 1,2; so the two channels and l l is the length of the flow path of the doublet which is assumed to be the same in both channels. Lets define the pressure difference in the different points that matters. At first the pressure difference between wetting phase,$\mathbf{P_w}$, and the pressure for wetting phase at the interface, $\mathbf{P_{wi}}$. This gives;

$$\mathbf{\Delta P_w - Pwi} = \frac{\mathbf{128 \mu_w l q_1}}{\pi \mathbf{D_1^4}} \tag{8}$$

For the other side of the doublet the same equation can be made, only here it is a non-wetting phase which is given with subscript nw.

$$\mathbf{\Delta P_{nwi} - P_{nw}} = \frac{\mathbf{128 \mu_{nw} l q_1}}{\pi \mathbf{D_1^4}} \tag{9}$$

The velocity of the interface boundary movement in capillaries 1 and 2 is influenced by the magnitude of the capillary pressure across the interface boundary, this gives equation

$$\mathbf{\Delta P_c} = (\mathbf{P_{nw} - P_w}) = \frac{\mathbf{4\sigma cos(\theta_A)}}{\mathbf{D_1}} \tag{10}$$

where σ is the interfacial tension and $\theta_\mathbf{A}$ the contact angle.
To simplify the next assumptions is made; $\mu_\mathbf{w} = \mu_\mathbf{nw} = \mu$. With this known and equation 8,9 and 10 the overall pressure can be expressed

$$\mathbf{\Delta P_B - P_A} = -\frac{\mathbf{128 \mu l q_1}}{\pi \mathbf{D_1^4}} + \frac{\mathbf{4\sigma cos(\theta_A)}}{\mathbf{D_1}} \tag{11}$$

For the second pore equation similar steps are done, this gives the equation below

$$\mathbf{\Delta P_B - P_A} = -\frac{\mathbf{128 \mu l q_2}}{\pi \mathbf{D_2^4}} + \frac{\mathbf{4\sigma cos(\theta_A)}}{\mathbf{D_2}} \tag{12}$$

The overall pressure change is same for both pores, therefore:

$$-\frac{\mathbf{128 \mu l q_1}}{\pi \mathbf{D_1^4}} + \frac{\mathbf{4\sigma cos(\theta_A)}}{\mathbf{D_1}} = -\frac{\mathbf{128 \mu l q_2}}{\pi \mathbf{D_2^4}} + \frac{\mathbf{4\sigma cos(\theta_A)}}{\mathbf{D_2}} \tag{13}$$

Equations 7 through 13 were used to solve for $\mathbf{q_1}$ and $\mathbf{q_2}$ as functions of $\mathbf{q_w}, \mathbf{D_1}, \mathbf{D_2}, \mu, \mathbf{l}$ and $\mathbf{\Delta P_c}$. In order to obtain an expressions of the velocity, each q is divided by its respective cross sectional area,

$$\frac{\pi \mathbf{D_j^2}}{\mathbf{4}} \tag{14}$$

Now the overall pressure change over the two pores is:

$$-\frac{\mathbf{8 \mu l v_1}}{\pi \mathbf{R_1^4}} + \frac{\mathbf{2\sigma cos(\theta_A)}}{\mathbf{R_1}} = -\frac{\mathbf{8 \mu l v_2}}{\pi \mathbf{R_2^4}} + \frac{\mathbf{2\sigma cos(\theta_A)}}{\mathbf{R_2}} \tag{15}$$

From equation 15 a relation between v_1 and v_2 can be made:

$$\mathbf{v_1} = \frac{\mathbf{r_1^2}}{\mathbf{r_2^2}} \mathbf{v_2} - \frac{\sigma \mathbf{cos(\theta) r_1^2}}{\mathbf{4 \mu l}} \left(\frac{\mathbf{1}}{\mathbf{r_2}} - \frac{\mathbf{1}}{\mathbf{r_1}} \right) \tag{16}$$

For v_1 to be positive (no trapping by bypassing), it must satisfy the next condition:

$$\mathbf{v_2} > \frac{\sigma \mathbf{cos(\theta) r_2^2}}{\mathbf{4 \mu l}} \left(\frac{\mathbf{1}}{\mathbf{r_2}} - \frac{\mathbf{1}}{\mathbf{r_1}} \right) \tag{17}$$

The values of v_2 needed to make v_1 positive. At reservoir type velocities, v_1 will not be positive and oil will be displaced only from the smaller pore. Once the water breaks through at the other end of the pore doublet, the oil in the larger pore is trapped and very difficult to mobilize.

Jamin-effect

Assume the a static system with different pressures between point A and B, this is due to the capillary forces. In order that the oil blob flows through the pore throat the static pressure difference must be exceeded, in other words must overcome to initiate flow.

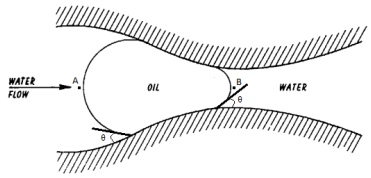

Fig. 27. Oil droplet that entering a pore constriction, with addition of point taken for governing equation on jamin effect [McAuliffe et al. 1973]

For the governing equation the following assumption is made, the pressure within the oil droplet is constant over the whole droplet. We then get the following equations:

$$\mathbf{P_A} + \left(\frac{\mathbf{2\sigma_{ow}cos\theta}}{\mathbf{r}}\right)_{\mathbf{A}} - \left(\frac{\mathbf{2\sigma_{ow}cos\theta}}{\mathbf{r}}\right)_{\mathbf{B}} = \mathbf{P_B} \quad (18)$$

This is equal to

$$\mathbf{P_A} - \mathbf{P_B} = \left(\frac{\mathbf{2\sigma_{ow}cos\theta}}{\mathbf{r}}\right)_{\mathbf{B}} - \left(\frac{\mathbf{2\sigma_{ow}cos\theta}}{\mathbf{r}}\right)_{\mathbf{A}} \quad (19)$$

This is the pressure drop holding the oil droplet in this pore. If we want to move the oil droplet, PA needs to exceed this pressure drop or no flow will happen.

B. APPENDIX B

The protocols for reproduction of the experiments in this paper.

Operational Protocol

(1) *Always wear a lab coat*
Beside it is necessary for safety, lab coat is also repellent of dust.

(2) *Always wear nitrile gloves*
By wearing these gloves the grease of our hands will not come in contact with the setup and specifically the micromodel

(3) *Filtrate all the liquids*
By filtrating the liquid all particles will be sieved out and not clog the microchip.

(4) *Clean all the syringes before use*
To make sure there are no particles left behind that can come into the system and cause a blockage.

Start-up protocol experiments

(1) *Flush pipes/connections/filters with water and afterwards dry it in compressed air*
The equipment is cleaned an extra time so the risk of any pollution in the system will be reduced

(2) *Do a leak test, when set-up is connected*
This bubble test is possible due to the fact CO2 flooding will occur during the experiment.

Running Experiments

(1) *Turn on the camera*
Now it is possible to gather images during the experiments

(2) *Inject CO_2 in the system for 15 min at a pressure of 8 - 10bar*
CO_2 can be dissolved in the brine. Thanks to this feature it is possible to reach 100% saturation in the microchip.

(3) *Start injection of Brine*
An injection speed of 0.1 μl/min and a total of 10 times the pore volume has to be inject in the micromodel.

(4) *Start injection of dyed Dodecane*
When starting the injection, remember that first all the brine in the tubing has to pass through the set-up before the oil can reach the microchip inlet. The injection speed remains 0.1 μl/min and a total of 10 times the pore volume has to be inject in the micromodel. At this point a reservoir condition is mimicked

(5) *Start actual experiment waterflooding*
Start injection brine in order to mimic waterflooding. The injection speed should be set at reservoir condition, 1 ft a day. The total length of the microchip is 79 cm = 2.59 ft, so it should take 2.6 days to go through the chip. With a pore volume of 18 μl it means that an injection speed of 0.29 μl/hour or 4.8 nl/min is required. This is not possible using the syringe pump that was available. An injection speed of 0.1 μl/min was therefore used in these experiments.

(6) *Start injection of surfactant*
Start injection of the surfactant at the same speed as the waterflooding was done

Cleaning protocol

The mircochips are designed so that it will hold the oil and water good in the system. Nevertheless it has to be cleaned completely, this is due to the salt present. If the salt gets crystallised, the chip may get clogged.

(1) *Inject of demi water*
Start with a low injection speed of 0.5 μl a minute and a total of 10 times the volume. After that the injection speed is set to 1l a minute and a total of 5 times the volume.

(2) *Inject of propanol*
Start with a low injection speed of 0.5μl a minute and a total of 10 times the volume. After that the injection speed is set to 1l a minute and a total of 5 times the volume.

(3) *Inject of demi water*
Start with a low injection speed of 0.5μl a minute and a total of 10 times the volume. After that the injection speed is set to 1l a minute and a total of 5 times the volume.

(4) *Drying in high temperature oven*
Put the microchip on a flat surface so that it cannot bend during the drying. The oven is set at 500 ^{o}C, with a build-up of 3 hours and it stays there for an hour.

An other possibility is to store the micromodel after experiments in a tank filled with demi-water. Then there is no possibility of formation of salt as it is submerse in demi-water, only problem is when doing new experiments your micromodel is filled with different fluids.

C. APPENDIX C

Here the specific design information of the micromodel can be found. [Schlautmann et al. 2007] The dimension of the glass chip is 90X30mm where the specific design is wet etched out. Wet etching of glass is an isotropic etching technique. This means that the width of the channels is more than twice the depth of it, and that the corners are rounded. The bottom of the channel stays smooth and optically transparent. [Micronit 2015] With this technique two glass plate are wet etched and then sealed together.
In Figure28 the layout of the pathway of the chip is shown. It has a total length of 79cm of the pore network.

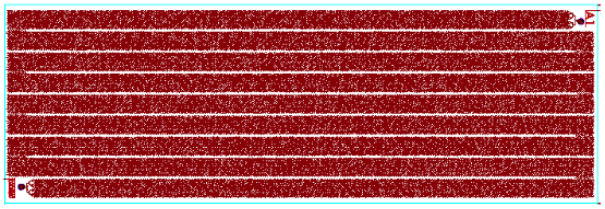

Fig. 28. Total wet etched pathway of the micromodel within the glass dimension of 90x30mm

Figure29 gives the cross section of the chip and its two layers of glass plate It is viewed from the top and looking through the device. There are two inlet/outlet visible, they are powder blasted holes that leads to the wet etched channels. The specific dimension of the chip can be found in the picture below.

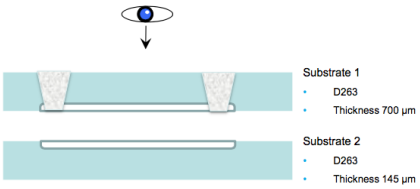

Fig. 29. Cross section of the chip with it specific dimension, with the two inlet/outlet and the wet etched channel.

Now the cross section of the channel is shown in Figure30. It shows more the ingenuity of the wet etched channel and it specific dimension. In this example the cross section of the throat with $12\mu m$ is displayed. This is one of the four different throat sizes, more is explained in figure31

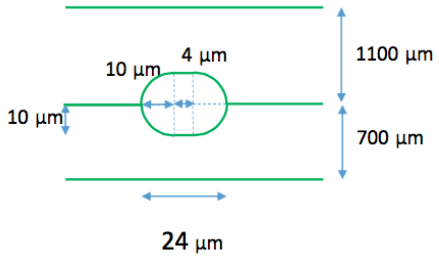

Fig. 30. Cross section of a $12\mu m$ throat and its specific dimension

The complexity of this micromodel is the heterogeneity of the pore structure. A total of 4 throat sizes and 9 Pore sizes is used within this model. A section of this structure is shown in figure31, there the specific dimension of the throats and pores can be found. It shows the mask area, this is the area of the chip that is bend in the corners as shown in figure30. The radius is the specific distance between these corners of the etched out section.

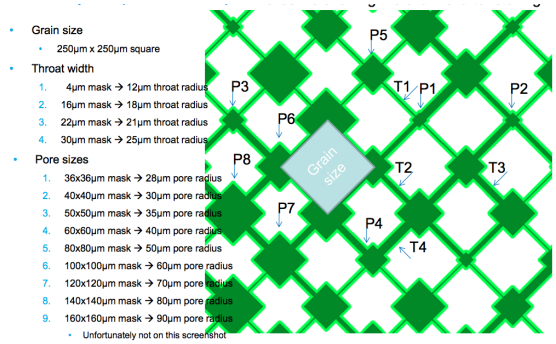

Fig. 31. Pore and throat distribution of the micromodel with it specific dimensions. It is missing the pore size 9

Theoretical permeability calculation of each pore within the micromodel is shown in tableVI The calculation is based on equation 4

Table VI. Theoretical permeability calculation of each pore within the micromodel

Pore number	Pore Radius $[\mu]m$	Permeability $[m^2]$
1	28	6.53E-11
2	30	7.50E-11
3	35	1.02E-10
4	40	1.33E-10
5	50	2.08E-10
6	60	3.00E-10
7	70	4.08E-10
8	80	5.33E-10
9	90	6.75E-10

For the pore throat within the theoretical permeability calculation the weighted average was taken over the 4 different size. The permeability of each pore throat is shown in tableVII this gives a harmonic average of $8.91E-12m^2$

Table VII. Theoretical permeability calculation of each pore throat within the micromodel

Throat number	Pore Throat Radius $[\mu]m$	Permeability $[m^2]$
1	12	4.50E-12
2	18	1.01E-11
3	21	1.38E-11
4	25	1.80E-11

Micromodel Chipholder

The old and new design of the micromodel holder is displayed below.

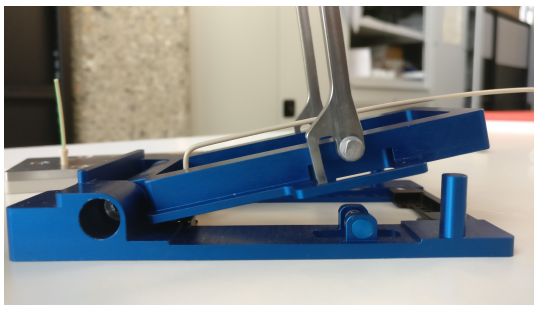

Fig. 32. The original Micromodel Holder, were there is a limitation in the pressure within the system

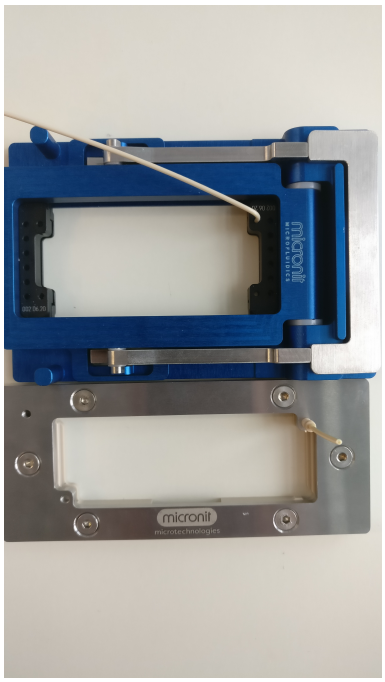

Fig. 33. The original Micromodel Holder and the newly designed micromodel holder with top view. Where the new holder has screw to clam the Peek tubing

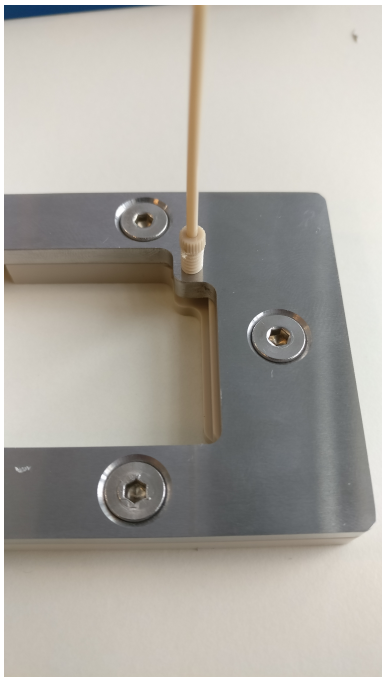

Fig. 34. A closer view of the newly micromodel holder with the screw.

D. APPENDIX D

Will be later added, the program I use for Latex, overleaf, can't handle the high quality images.

Saturation of each position

The saturation of the oil is displaced for each position on the micromodel. The upper image displays the initial oil saturation and the lower image the residual oil saturation. Here the images are only enhanced with local contrast.

Position 8
From the analysis it can be determined that the saturation of position 8 after waterflooding is 45.8% compared to the initial oil saturation of 57.4%. This gives a recovery factor of 20.2%

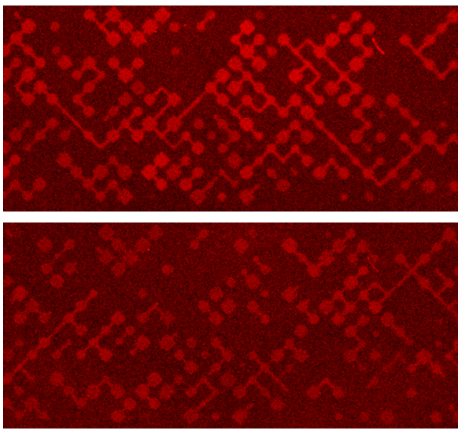

Fig. 35. Oil saturation on position 8. The top network is before waterflooding, bottom is after waterflooding.

Position 7
From the analysis it can be determined that the saturation of position 7 after waterflooding is 39.6% compared to the initial oil saturation of 58.2%. This gives a recovery factor of 32.0%

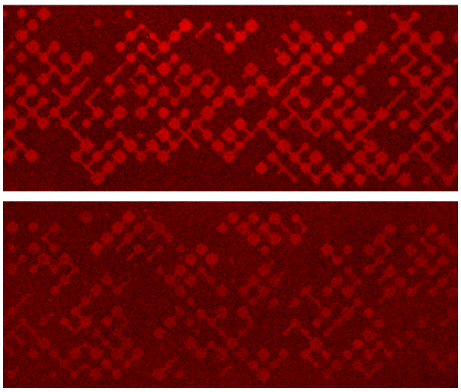

Fig. 36. Oil saturation on position 7. The top network is before waterflooding, bottom is after waterflooding.

Position 6

From the analysis it can be determined that the saturation of position 6 after waterflooding is 48.5% compared to the initial oil saturation of 60.2%. This gives a recovery factor of 19.3%

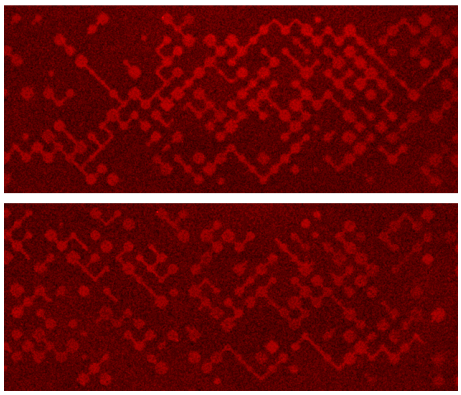

Fig. 37. Oil saturation on position 6. The top network is before waterflooding, bottom is after waterflooding.

Oil ganglion size network

Here the network of the oil ganglia are show, again upper image displace the before waterflooding, bottom after waterflooding. With their corresponding cumulative graph

Position 8

In figure 39 the cumulative distribution of the oil ganglion size is shown, the data was generate out of figure 38. A clear gap between the before and after waterflooding curves is seen. This shows that there is an increase in smaller oil ganglia.

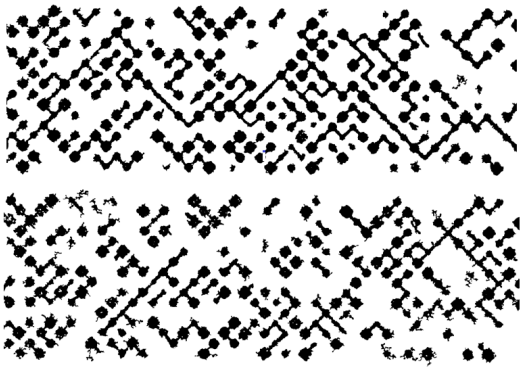

Fig. 38. Oil saturation on position 8. The top network is before waterflooding, bottom is after waterflooding.

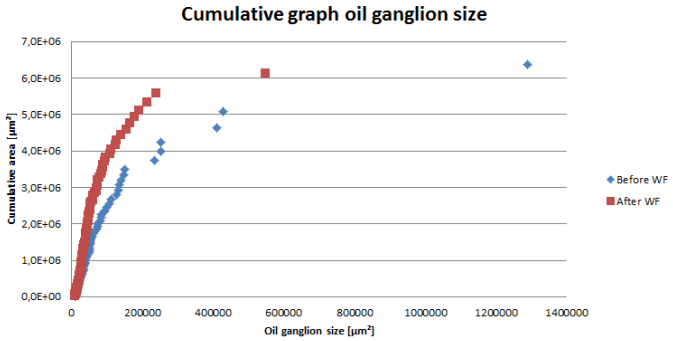

Fig. 39. Cumulative curve of the oil ganglion size before and after waterflooding for position 8

Position 7

In figure 41 the cumulative distribution of the oil ganglion size is shown, the data was generate out of figure 40. A clear gap between the before and after waterflooding curves is seen. This shows that there is an increase in smaller oil ganglia.

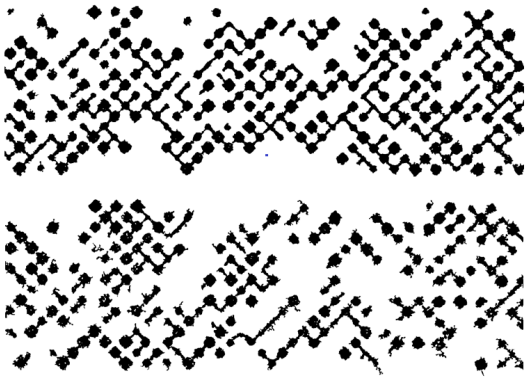

Fig. 40. Oil saturation on position 7. The top network is before waterflooding, bottom is after waterflooding.

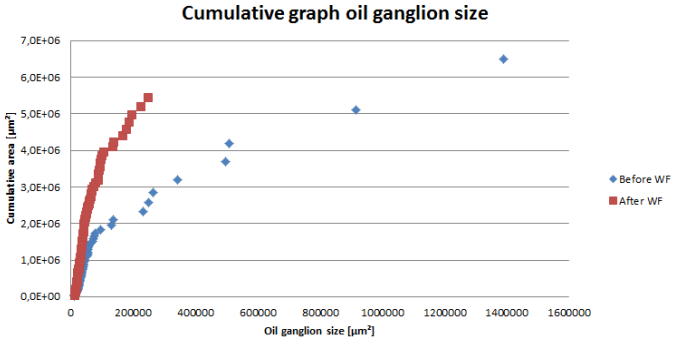

Fig. 41. Cumulative curve of the oil ganglion size before and after waterflooding for position 7

Position 6

In figure 43 the cumulative distribution of the oil ganglion size is shown, the data was generate out of figure 42. A clear gap between the before and after waterflooding curves is seen. This shows that there is an increase in smaller oil ganglia.

Fig. 42. Oil saturation on position 6. The top network is before waterflooding, bottom is after waterflooding.

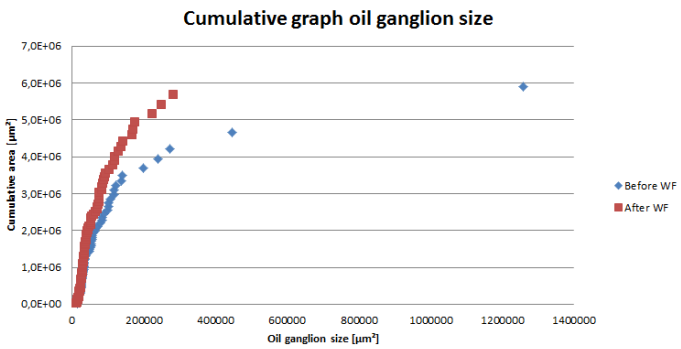

Fig. 43. Cumulative curve of the oil ganglion size before and after waterflooding for position 6

Position 5

In figure 45 the cumulative distribution of the oil ganglion size is shown, the data was generate out of figure 44. A clear gap between the before and after waterflooding curves is seen. This shows that there is an increase in smaller oil ganglia.

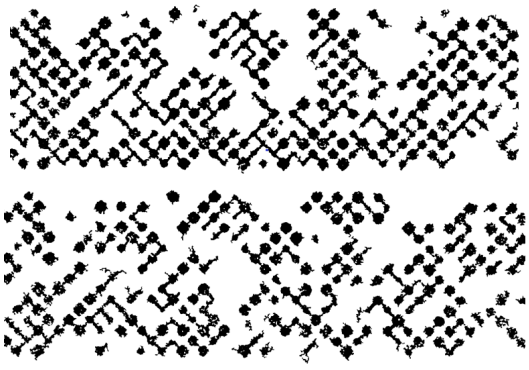

Fig. 44. Oil saturation on position 6. The top network is before waterflooding, bottom is after waterflooding.

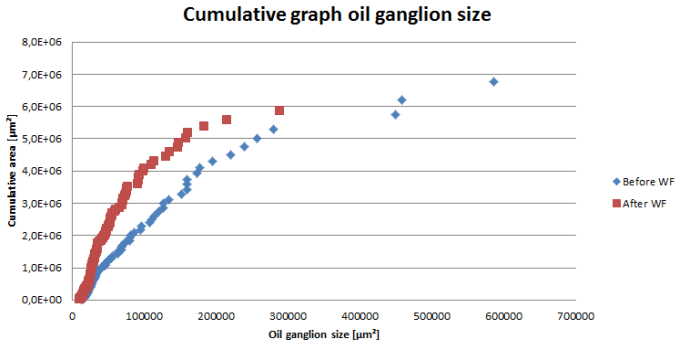

Fig. 45. Cumulative curve of the oil ganglion size before and after waterflooding for position 5

Velocity images

Displaying an image sequence of the propagation of two different oil ganglion during the waterflooding period. The oil ganglion is highlighted with a yellow contour.

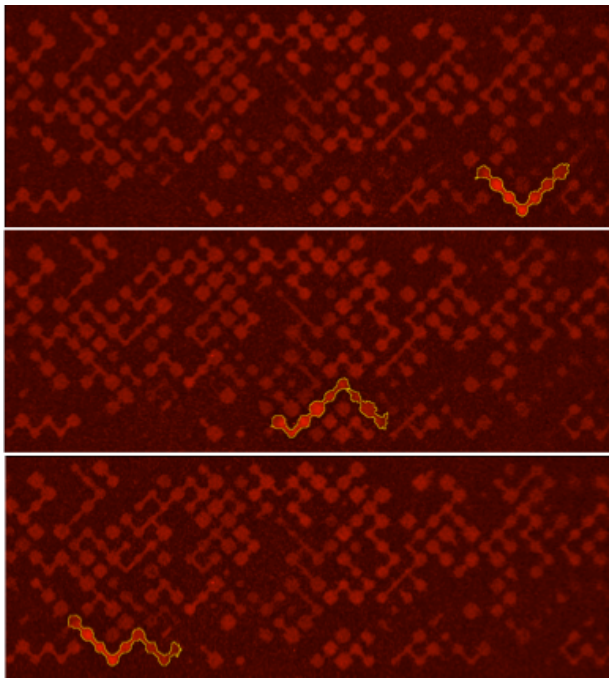

Fig. 46. The propagation of an oil ganglion, size $0.187mm^2$ indicated with yellow line, with the upper image at time = 0 s, the middle at time = 8 s and the lower image at time = 17 s. Giving a velocity of $0.187\mu m/s$

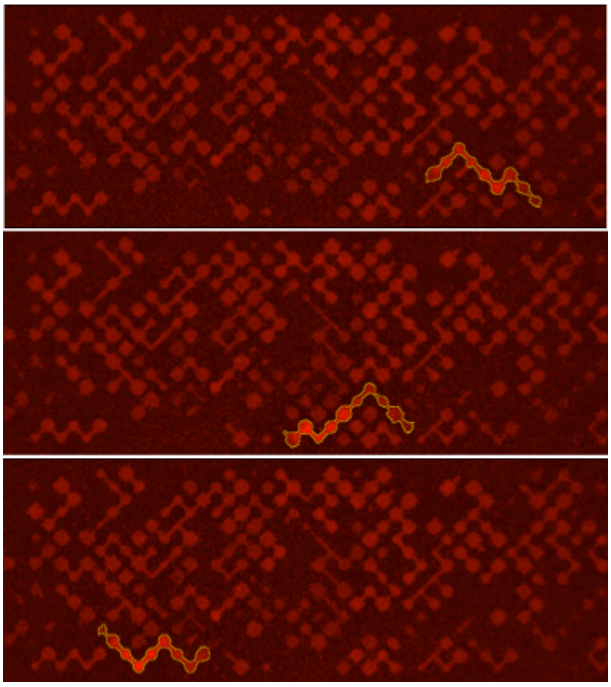

Fig. 47. The propagation of an oil ganglion, size $0.235mm^2$ indicated with yellow line, with the upper image at time = 0 s, the middle at time = 6 s and the lower image at time = 14 s. Giving a velocity of $0.235\mu m/s$